

L1 data fitting for robust reconstruction in magnetic particle imaging: quantitative evaluation on Open MPI dataset

Tobias Kluth and Bangti Jin

Abstract—Magnetic particle imaging is an emerging quantitative imaging modality, exploiting the unique nonlinear magnetization phenomenon of superparamagnetic iron oxide nanoparticles for recovering the concentration. Traditionally the reconstruction is formulated into a penalized least-squares problem with nonnegativity constraint, and then solved using a variant of Kaczmarz method. In order to achieve good performance, a preprocessing step of frequency selection to remove the deleterious influences of highly noisy measurements is often adopted. In this work, we propose a complementary approach to frequency selection, by viewing highly noisy measurements as outliers, and employing the L1 data fitting, one popular approach from robust statistics. When compared with the standard approach, it is easy to implement with a comparable computational complexity. Experiments with a public domain dataset, i.e., Open MPI dataset [1], show that it can give accurate reconstructions, and is less prone to noisy measurements, which is clearly illustrated by the quantitative (PSNR / SSIM) and qualitative comparisons with the standard approach.

Index Terms—magnetic particle imaging, frequency selection, image reconstruction, L1 norm

I. INTRODUCTION

Magnetic particle imaging (MPI), invented by Gleich and Weizenecker in 2005 [2], is a relatively new medical imaging modality. It exploits the unique nonlinear magnetization behavior of super-paramagnetic iron oxide nanoparticles in an applied magnetic field. In the experiment, a static magnetic field (selection field), given by a gradient field, generates a field free point (FFP) (or a field free line (FFL) [3]), and its superposition with a spatially homogeneous but time-dependent field (drive

Manuscript received January 14, 2020.

T. Kluth is with Center for Industrial Mathematics, University of Bremen, Bibliothekstr. 5, 28357 Bremen, Germany (tkluth@math.uni-bremen.de). T. Kluth acknowledges funding by the Deutsche Forschungsgemeinschaft (DFG, German Research Foundation) - project number 281474342/GRK2224/1 “Pi³ : Parameter Identification - Analysis, Algorithms, Applications” and support by the project “MPI²” funded by the Federal Ministry of Education and Research (BMBF, project no. 05M16LBA).

B. Jin is with Department of Computer Science, University College London, Gower Street, London WC1E 6BT, UK (b.jin@ucl.ac.uk, bangti.jin@gmail.com). The work of B. Jin is partly supported by UK EPSRC EP/T000864/1.

field) moves the field free region along a predefined trajectory defining the field-of-view. The change of the applied field causes a change of the nanoparticle magnetization, which can be measured for recovering the spatially dependent concentration of nanoparticles. See the surveys [4], [5], [6] for relevant physics, instrumentation and mathematical modeling.

In comparison with more traditional imaging modalities, e.g., ultrasound, MRI and PET, MPI has a number of distinct features: high temporal / spatial resolution, high sensitivity and free from the need of harmful radiation. Thus it is especially attractive for *in-vivo* applications, and the list of potential medical applications is long and fast growing, including imaging blood flow [7], long-term tracer monitoring [8], estimating potential flow [9], tracking medical instruments [10], tracking and guiding instruments for angioplasty [11], cancer detection [12] and cancer treatment by hyperthermia [13].

Hence, the MPI reconstruction problem is of great importance, and has received much attention [7], [14], [15], [16], [17], [18], [19], [20], [21], [22], [23], [24] (see [5] for an overview). Roughly, existing approaches can be categorized into two groups, i.e., data-based v.s. model-based, dependent of the description of the forward map. The former uses a measured forward map, whereas the latter employs a mathematical model to describe the forward map, where the equilibrium model based on Langevin theory is popular [6], [25]. The data-based approach is predominant in practice, since it can deliver better quality reconstructions.

The starting point of this study is the following empirical observation: the recorded signal often contains a significant amount of frequency-dependent anomalies. In Fig. 1, we show the variance of background measurements provided with the “shape” phantom from Open MPI dataset [1] (available at www.tuhh.de/ibi/research/open-mpi-data.html, accessed on September 20, 2019) acquired at *x*- and *y*-receive coils. It is observed that the variance of some data points is huge and deviate enormously from the bulk (noting the log scale for *y*-axis) in both real and imaginary parts and do not follow an independent and identically distributed (i.i.d.)

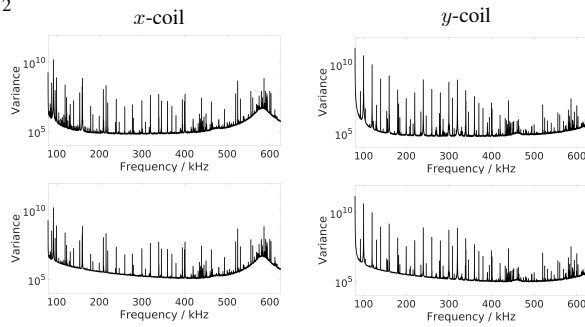


Fig. 1: Variance of the background measurement for the “shape” phantom. Visualized individually for x and y receive coils with respect to the frequency; real part (top), imaginary part (bottom).

Gaussian model. In practice, they are often deemed data “noise”, and an important question in image reconstruction is how to deal with such noise.

Often the data-based image reconstruction in MPI proceeds as follows. First, one selects a number of frequencies based on a suitable “signal-to-noise ratio (SNR)” criterion [19], and discards the remaining frequencies; see Section II-A for details. This step partly removes the nongaussian component of the noise. The reconstruction is performed using only the selected frequencies, often formulated into a penalized least-squares problem with nonnegativity constraint and solved by a variant of Kaczmarz method [26]. This strategy has achieved great empirical success, and is now a standard MPI reconstruction algorithm.

Nonetheless, there are still several issues on the overall procedure. First, frequency selection is *ad hoc* in nature, since the threshold τ is nontrivial to set due to dependence on background noise, while exerts big effect on imaging quality. A too large τ may throw away informative data points, whereas a too small τ may invalidate i.i.d. Gaussian assumption of the ℓ^2 fitting. Second, the performance relies on hybrid regularizing effects of both penalty and early stopping of Kaczmarz iteration (e.g., a few sweeps over the data), and the delicate interplay has not been fully exposed. The hybridization greatly complicates the choice of the regularization parameter and the stopping index. Third and last, the modeling errors in the measured forward map are often not fully accounted for, even though there are important efforts in that direction [21], [22]. This issue is related to the proper mathematical modeling in MPI and is fundamental towards an accurate model-based reconstruction algorithm (see [27] for recent progress).

In this work, we present a complementary approach to SNR type frequency selection which partly addresses the first challenge raised above. It is based on the standard ℓ^1 data fitting, or equivalently a Laplace model on the

noise (see Section II-B for details), which has been popular in several areas, e.g., signal processing [28] and image processing [29], but it has not been applied to MPI reconstruction yet, to the best of our knowledge. The rational is that the nonselected frequencies deviate largely from the bulk of the signals and thus can be viewed as outliers, and ℓ^1 fitting is known to be more robust with respect to outliers than the ℓ^2 fitting [30]. The approach allows adaptive use of the data and thus full exploitation of the given data for better reconstructions. Numerically, ℓ^1 fitting leads to a convex but nonsmooth optimization problem, which can be solved efficiently by many modern stand-alone optimization solvers. We employ a popular variant of the limited memory BFGS algorithm, i.e., L-BFGS-B [31], [32]. We carry out extensive numerical experiments with Open MPI dataset. Our findings include that the ℓ^1 approach can indeed yield excellent reconstructions both quantitatively in terms of PSNR and SSIM and qualitatively in terms of background and sharpness. The ℓ^1 approach is able to compete with the standard iterative Kaczmarz-type approach which yields high quality MPI reconstructions when using small numbers of iterations, while the variational ℓ^2 approach fails. Thus, these techniques may facilitate fast and accurate MPI reconstruction using variational regularization techniques. To the best of our knowledge, this is the first work presenting quantitative results for phantom MPI data.

The rest of the paper is organized as follows. In Section II, we motivate and develop the robust formulation, and describe the limited-memory BFGS algorithm. In Section III, we present extensive quantitative and qualitative numerical results to showcase the performance of the proposed approach. In Section IV, we give concluding remarks and further discussions. In the supplements, we provide additional numerical results.

II. METHODOLOGIES

In this part we describe the standard approach and develop the ℓ^1 approach.

A. Standard approach

The now standard preprocessing approaches to treat the noise is frequency selection, including band pass approach and SNR-type thresholding. The description of these approaches below largely follows [23]. Let $J_{\text{BP}} = \{j \in \mathbb{Z} \mid b_1 \leq |j|/T \leq b_2\}$ be the indices for frequency band limits $0 \leq b_1 < b_2 \leq \infty$ and measurement time T . This step is to further filter out remaining signal contributions of the analogously filtered direct feedthrough induced by the applied magnetic field. For SNR-type thresholding, one standard quality measure is the ratio of mean absolute values from individual measurements $v_\ell^{(i)}$ (for the i -th calibration scan at

the ℓ -th receive coil) and empty scanner measurements $\{v_{\ell,0}^{(k)}\}_{k=1}^K$ [33]. Specifically, let $I_{\text{SNR}} \subset \{1, \dots, N\}$ be the index set of individual measurements. Let $\{\psi_j\}_{j \in \mathbb{N}}$ be an orthonormal basis, e.g., discrete Fourier basis, for $L^2(I)$, where I is the time interval for measurement. Then we define

$$d_{\ell,j} = \frac{\frac{1}{|I_{\text{SNR}}|} \sum_{i \in I_{\text{SNR}}} |\langle v_{\ell}^{(i)} - \mu_{\ell}^{(i)}, \psi_j \rangle|}{\frac{1}{K} \sum_{k=1}^K |\langle v_{\ell,0}^{(k)} - \mu_{\ell}, \psi_j \rangle|}, \quad (\text{II.1})$$

where $\mu_{\ell} = \frac{1}{K} \sum_{k=1}^K v_{\ell,0}^{(k)}$ is the mean background measurement, and $\mu_{\ell}^{(i)} = \kappa_i v_{\ell,0}^{(k_i)} + (1 - \kappa_i) v_{\ell,0}^{(k_i+1)}$ is a convex combination of the k_i -th and $k_i + 1$ -th empty scanner measurements for the i -th calibration scan. The parameters $\kappa_i \in [0, 1]$ are chosen to be equidistant for all calibration scans between two consecutive empty scanner measurements. For a given threshold $\tau \geq 0$, we define

$$J_{\ell} = \{j \in J_{\text{BP}} \mid d_{\ell,j} \geq \tau\}, \quad \ell = 1, \dots, L, \quad (\text{II.2})$$

which comprises all frequency indices within a certain frequency band and fulfilling an SNR-type measure for the ℓ -th receive coil. The threshold τ determines the size of the reduced system and its accuracy: with a large τ , the procedure is more conservative but may erroneously remove informative data, whereas with a small τ , it may risk including highly corrupted data points. In Fig. 2, we present the SNR-type frequency selection with three thresholds. With a proper τ , the number of outliers is reduced, but not completely removed, even for $\tau = 5$, which may still greatly influence the reconstruction.

After applying band passing and thresholding, we obtain a (reduced) linear system

$$Ax = y, \quad (\text{II.3})$$

where A is the measurement matrix, and y is the noisy data. The standard approach in the MPI literature employs an l2 data fitting, which leads to the following constrained approach

$$\min_{x \geq 0} \frac{1}{2} \|Ax - y\|^2 + \frac{\alpha}{2} \|x\|^2, \quad (\text{II.4})$$

where $\|\cdot\|$ denotes the Euclidean norm, and $\alpha > 0$ is the penalty parameter, controlling the tradeoff between data fitting and penalty [34]. The constraint $x \geq 0$ is interpreted componentwise. Problem (II.4) is often minimized by a variant of Kaczmarz method [5]. In practice, dimension reduction techniques (via SNR type criterion or randomized SVD) and proper weighting [19], [23] may also be incorporated to accelerate and enhance the reconstructions.

Note that the discussion so far assumes that background subtraction has been carried out so that the noise has a zero mean, which is also assumed below. This condition is implicit in the standard formulation

(II.4). If the mean of the noise is nonzero, then the l2 fitting should incorporate the mean as a drift term. The influence of background subtraction differs from calibrating the noise statistics, e.g. whitening and heavy-tailed modeling. In practice, background subtraction is not always direct; see the works [35], [36], [37] for in-depth study, including joint estimation of the background and foreground.³

B. L1 fitting

Statistically, the formulation (II.4) assumes an i.i.d. Gaussian noise with zero mean. This is often justified by appealing to a version of central limit theorems, i.e., the Gaussian is suitable for data that are formed from the sum of a large number of independent components. A well known limitation of the Gaussian model formulation is its lack of robustness against outliers, i.e., data points that lie far away from the bulk of the data: A single aberrant data point can greatly influence all the parameters in the model, even for these with little substantive connection to the outlying observations [30, p. 443].

Thus, the validity of the approach (II.4) resides on validity of the i.i.d. Gaussian assumption on the noise. However, not all data in MPI can be adequately described by a Gaussian model. From Fig. 1, Gaussianity at best holds true only for some frequencies, whereas for the others, the data contains a significant amount of error, with outlier like noise. The precise mechanism for the noise remains largely elusive, and there are multiple sources, related to unmodeled physics of the experimental process, e.g., imperfect analog filter, direct feedthrough, and unexpected magnetization of scanner components. In practice, the electronic noise is often assumed to be Gaussian [38], which is then weighted with a transfer function, and also there exist (generally nongaussian) background noise artifacts; see [39] for a study on the noise sources in the receive chain of an MPI scanner. It is known in image processing [40], signal processing [28] and statistics [41] that noise with outliers is more adequately described by heavy-tailed distributions. In the presence of outliers, an inadvertent adoption of the Gaussian model can seriously compromise the reconstruction accuracy [30], and often does not allow full extraction of the information provided by the data. This calls for methods that are robust to outliers.

There are several ways to derive robust estimators. One classical approach is to first identify outliers with noise detectors, e.g., by adaptive median filter and nonlocal mean filter [42], [43], and then to perform inversion on the dataset with outliers excluded [30]. Frequency selection in Section II-A is a special noise detector (with an SNR type criterion). This approach depends on the accuracy of the noise detector. It can be highly nontrivial to accurately identify all outliers, and misidentification

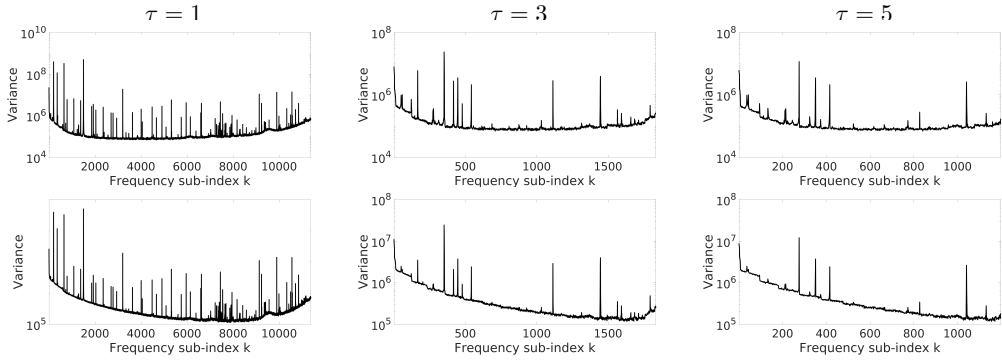


Fig. 2: Variance of the background measurement for the “shape” phantom. Visualized for the receive coil in x -direction for different thresholds τ versus frequency indices $j_k \in J_1$; real part (top), imaginary part (bottom).

can adversely affect the reconstruction quality. See Fig. 2 for an illustration. These observations necessitate developing more systematic strategies for handling outliers, which can be achieved by modeling them explicitly with a heavy-tailed distribution, e.g., Laplace, Student t and Cauchy [44]. Laplace distribution is one most popular choice, with its density $p(\xi)$ in one-dimension given by

$$p(\xi) = \frac{\lambda}{2} e^{-\lambda|\xi-\mu|},$$

where μ and $\lambda > 0$ denote the mean (location) and (inverse) scale, respectively.

The proposed approach is based on an i.i.d. Laplace distribution with zero mean assumption on the noise, so as to allow outliers in the data. Assuming a Gaussian prior in the Bayesian formalism as in (II.4) and then considering the maximum a posteriori estimator lead to

$$\min_{x \geq 0} \|Ax - y\|_1 + \frac{\alpha}{2} \|x\|^2, \quad (\text{II.5})$$

where the notation $\|\cdot\|_1$ denotes the ℓ^1 norm, i.e.,

$$\|z\|_1 = \sum_i |z_i|,$$

and the scalar $\alpha > 0$ is the corresponding regularization parameter. In the absence of nonnegativity constraint, this model was analyzed in [29].

The difference of (II.5) from (II.4) is that it employs the ℓ^1 fitting, which is more robust to outliers, i.e., the outliers influence less the reconstructions, instead of the usual ℓ^2 fitting. It partly avoids the frequency selection step in the two-step procedure, and allows using more systematically the given data. In passing, one may also employ the student t distribution or Huber’s robust statistics, but they will not be explored below.

C. Numerical algorithm

The formulation (II.5) involves solving a convex but nonsmooth constrained optimization problem, and it can

be solved efficiently in several different ways, e.g., iteratively reweighted least-squares [45], alternating direction method of multipliers [46], semismooth Newton method [29] and limited-memory BFGS. These algorithms are easy to implement and converge steadily, if relevant tuning parameters are properly chosen. We employ a version of limited-memory BFGS, i.e., L-BFGS-B [31], [32]. It can ensure that problem (II.5) is solved accurately in the sense of optimization, i.e., finding a near global minimizer, so as to avoid extra regularizing effect from the optimizer due to early stopping.

Limited-memory BFGS-B is a popular quasi-Newton type method using a limited amount of computer memory for a differentiable objective function, approximating the inverse Hessian matrix using the BFGS approximation, and handling the simple box constraint (i.e., upper and lower bounds) by an active set type strategy [31]. It also includes a line search step to safeguard the progress, and speeds up the computation using a compact representation of the BFGS Hessian approximation. It is well suited for large-scale optimization problems with simple constraint, and there are several well tested implementations [32] (see <https://github.com/stephenbeckr/L-BFGS-B-C> for a MATLAB wrapper).

Since the ℓ^1 fitting is nondifferentiable, we approximate (II.5) by

$$\min_{x \geq 0} \|Ax - y\|_{1,\epsilon} + \frac{\alpha}{2} \|x\|^2,$$

where $\epsilon > 0$ is small, and $\|\cdot\|_{1,\epsilon}$ is defined by

$$\|v\|_{1,\epsilon} = \sum_i \sqrt{v_i^2 + \epsilon^2}.$$

Upon smoothing, the objective function is differentiable, and thus the limited memory BFGS-B can be applied directly. This smoothing is simple and easy to implement.

III. NUMERICAL EXPERIMENTS

Now we present numerical results to illustrate the potential and performance of the proposed ℓ^1 fitting

on real data. The experimental setup is as follows. We employ a measured system matrix, where a band pass filter is applied (with $b_1 = 80$ kHz and $b_2 = 625$ kHz) and frequency selection (with discrete Fourier basis $\{\psi_j\}_{j \in \mathbb{N}}$) with a SNR threshold τ is optionally applied, which yields a system matrix $A_\tau \in \mathbb{R}^{n \times m}$ for the $L = 3$ receive channels (see [23, Sec. 2.1] for the description). Optionally, A_τ can also be whitened [23, Sec. 2.3], where background measurements are used to obtain a diagonal whitening matrix $W_\tau \in \mathbb{R}^{n \times n}$. System matrices and measurements are concatenated and background-subtracted [23, Sec. 2.1]. For frequency selection, we consider four thresholds, i.e., $\tau = 0, 1, 3, 5$, and the corresponding number n of rows of A_τ is 70446, 68566, 9564 and 6146. All forward maps are scaled to have a unit operator norm.

Below we compare results obtained from the following reconstruction methods.

- **[I1-L]:** The 11 fitted reconstructions x_{11} and $x_{W;11}$ are respectively obtained by

$$x_{11} = \arg \min_{x \geq 0} \|A_\tau x - y^\delta\|_{1,\epsilon} + \frac{\alpha}{2} \|x\|^2 \quad \text{and}$$

$$x_{W;11} = \arg \min_{x \geq 0} \|W_\tau A_\tau x - W_\tau y^\delta\|_{1,\epsilon} + \frac{\alpha}{2} \|x\|^2,$$

where the minimization is performed with L-BFGS-B.

- **[I2-K, I2-L]:** The reconstructions x_{12} and $x_{W;12}$ are respectively obtained by

$$x_{12} = \arg \min_{x \geq 0} \frac{1}{2} \|A_\tau x - y^\delta\|^2 + \frac{\alpha}{2} \|x\|^2 \quad \text{and}$$

$$x_{W;12} = \arg \min_{x \geq 0} \frac{1}{2} \|W_\tau A_\tau x - W_\tau y^\delta\|^2 + \frac{\alpha}{2} \|x\|^2,$$

where I2-K denotes minimization by Kaczmarz method (see, e.g., [23, Algorithm 1]); respectively I2-L denotes minimization by L-BFGS-B.

These methods are evaluated on a public 3D dataset open MPI dataset (downloaded from <https://www.tuhh.de/ibi/research/open-mpi-data.html>, accessed on September 20, 2019) provided in the MPI Data Format (MDF) [47]. The system matrix data $\{v_\ell^{(i)}\}_{i=1}^m$, $\ell = 1, 2, 3$, is obtained using a cuboid sample of size 2 mm \times 2 mm \times 1 mm and a 3D Lissajous-type FFP excitation. The calibration is carried out with Perimag tracer with a concentration 100 mmol/l. The field-of-view has a size of 38 mm \times 38 mm \times 19 mm and the sample positions have a distance of 2 mm in x - and y -direction and 1 mm in z -direction, resulting in $19 \times 19 \times 19 = 6859$ voxels, which gives the number m of columns in the matrix A . The entries of A are averaged over 1000 repetitions and empty scanner measurements are performed and averaged every 19 calibration scans. The measurements are averaged over 1000 repetitions of the excitation sequence, and with each phantom, an empty measurement

with 1000 repetitions is provided, which are used for the background correction of the measurement and A [23, Sec. 2.1] and also for approximating the diagonal covariance C respectively the whitening matrix W [23, Sec. 2.3]. For the comparison below, the Kaczmarz method [23, Algorithm 1] is run for 200 iterations (one iteration means one loop over the entire dataset) if not otherwise stated. The L-BFGS-B algorithm in I1-L and I2-L is used with 20 limited-memory vectors, 1e-10 for pgtol, and 10000 for maximum number of iterations, and for I1-L, $\epsilon = 10^{-12}$ is chosen.

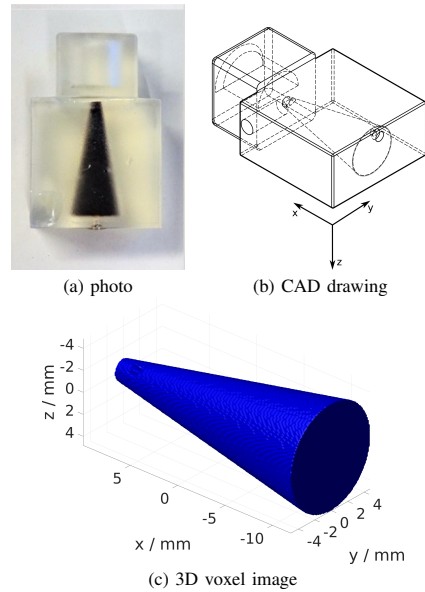


Fig. 3: “Shape” phantom from the open MPI dataset.

We validate the proposed method on the “shape” and “resolution” phantoms in the dataset. The “shape” phantom is a cone defined by a 1 mm radius tip, an apex angle of 10 degree, and a height of 22 mm. The total volume is 683.9 μ l. Perimag tracer with a concentration of 50 mmol/l is used. See Fig. 3 for a schematic illustration, where the plots are adapted from Open MPI dataset. The “resolution” phantom consists of 5 tubes filled with Perimag tracer with a concentration of 50 mmol/l. The 5 tubes have a common origin on one side of the phantom, and extend in different angles from the origin within the x - y - and y - z -planes. In the z -direction, the angles in the y - z -plane are chosen smaller (10 deg and 15 deg) than in x - y -plane (20 deg and 30 deg); see Fig. 4 for the illustration. In all the reconstructions below, the concentration unit is mmol/l. See Fig. 5 for the visualization structure of the 3D reconstructions below.

In the Open MPI dataset, CAD drawings of the phantoms are provided; see Figs. 3 and 4. This allows extracting voxel images as a ground truth reference.

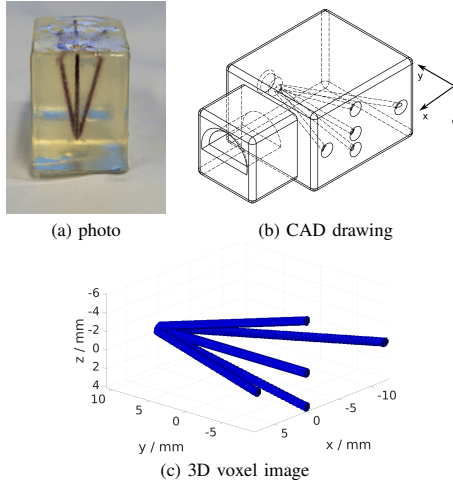


Fig. 4: “Resolution” phantom from the open MPI dataset.

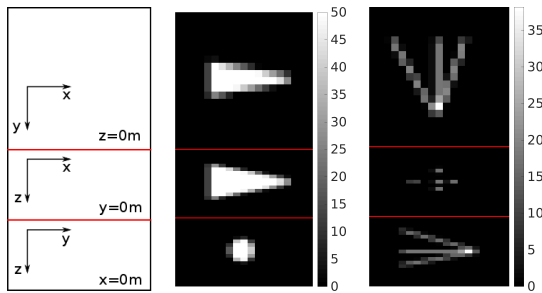


Fig. 5: Visualization structure for the 3D reconstructions (left) and the ground truth “shape” (middle) and “resolution” (right) phantoms on the spatial grid.

However, there is uncertainty with the actual phantom position, and also the robot arm moving the phantom in the bore has an unknown standard deviation. Thus, we formulate a conservative image quality measure as follows. First we estimate the phantom position from the reconstructed image to define a reasonable estimated reference image $c_0 : \mathbb{R}^3 \rightarrow \mathbb{R}_+$. Then we account for position uncertainty by shifts $\Delta r \in \mathcal{R}$, where \mathcal{R} is the set of all possible position shifts in the neighborhood $[-3\text{mm}, 3\text{mm}]^3$ with a step size 0.5mm in each direction ($|\mathcal{R}| = 2197$). The L^2 scalar products of $c_0(r + \Delta r)$ and the piecewise constant basis functions $\{\psi_j\}_j$ with respect to the voxel grid yields the reference image $x_{\text{ref}, \Delta r}$, which is then used to define the following conservative image quality measures

$$\epsilon_{\text{PSNR}}(x) = \max_{\Delta r \in \mathcal{R}} \text{PSNR}(x, x_{\text{ref}, \Delta r}) \quad (\text{III.1})$$

$$\epsilon_{\text{SSIM}}(x) = \max_{\Delta r \in \mathcal{R}} \text{SSIM}(x, x_{\text{ref}, \Delta r}) \quad (\text{III.2})$$

exploiting the standard image quality measures, i.e., peak-signal-to-noise-ratio (PSNR) and structural similar-

ity measure (SSIM) [48]. Two example reference images are illustrated in Fig. 5. These two metrics are used for quantitative comparisons below.

A. Algorithmic performance, quantitative comparison and the influence of SNR-type thresholding

First, we compare the performance of the methods quantitatively and qualitatively. To this end, we employ the best image quality measure for each method and SNR-type threshold τ , using the corresponding “optimal” regularization parameter α , and then visualize the respective reconstructions for a qualitative comparison. We analyze the measures PSNR and SSIM separately.

PSNR: The PSNR results are given in Table I; see Figs. 6 and 7 for the reconstructions. First, we compare the two pure variational regularization approaches 11-L and 12-L. Clearly, 11-L greatly outperforms 12-L in all cases, showing robustness of the 11 fitting with respect to outliers. Second, we compare 11-L to 12-K. The comparison with 12-K is difficult due to the interplay of two different sources of regularizing effect, i.e., variational and iterative, controlled respectively by α (in all methods) and iteration number K . Using a fixed and small K , as often done in practice, 12-K does not reach convergence in the sense of optimization (i.e., finding a global minimizer to (II.4)), and instead is actually early stopping in the spirit of iterative regularization [49]. However, for a sufficiently large K , the result by 12-K is similar to that by 12-L. This is clearly observed for the results for large thresholds τ . Now we examine the PSNR results more closely. For the “shape” phantom, 11-L performs better for larger τ thresholds and 12-K performs better for smaller τ . This observation also holds for the “resolution” phantom. The overall best possible PSNR is obtained by 11-L in both non-whitened and whitened cases (both for $\tau = 3$) for the “shape” phantom. For the “resolution” phantom, the optimum is achieved by 12-K in both cases (non-whitened: $\tau = 5$; whitened: $\tau = 1$), but only slightly higher than that by 11-L; see Section III-B for further results.

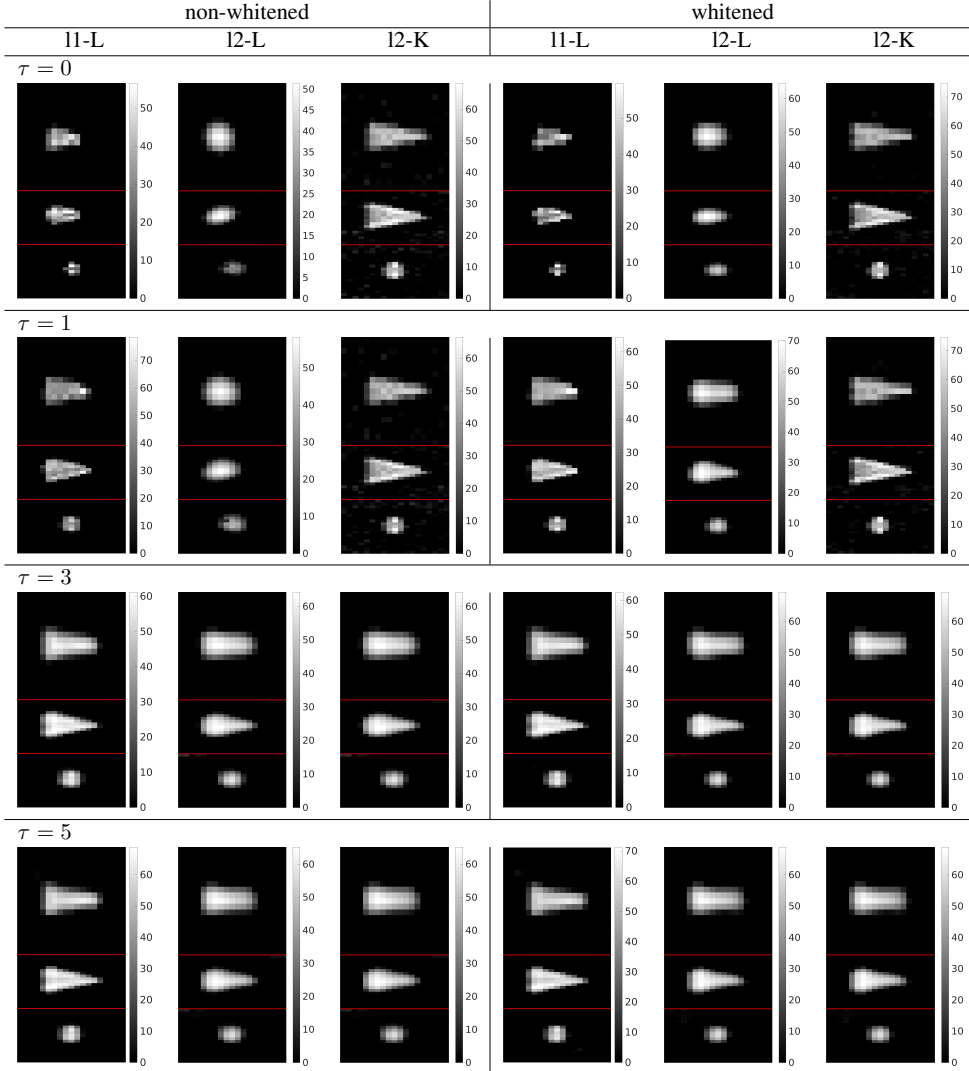
Qualitatively, the reconstructions in Figs. 6 and 7 (corresponding to the PSNR-optimal α) exhibit severe background artifacts for 12-K with small thresholds ($\tau = 0, 1$). 12-L fails to give reasonable results, and 11-L gives far more reasonable reconstructions for $\tau \geq 1$. For $\tau \geq 3$, 11-L reconstructions enjoy sharper edges and corners in the “shape” phantom compared to the competing methods. For the “resolution” phantom, 11-L and 12-K give similar results for $\tau \geq 3$, and both outperform 12-L.

SSIM: The SSIM results are given in Table II and the corresponding reconstructions in Figs. 8 and 9. Similar to the PSNR case, 11-L outperforms 12-L in all cases. In the non-whitened case, 11-L performs best for the “shape”

TABLE I: The ϵ_{PSNR} values for 11-L, 12-L, and 12-K (200 iterations).

τ	“Shape” phantom					
	non-whitened	whitened	12-K			
11-L	12-L	12-K	11-L	12-L	12-K	
0	19.687 (2^{-5})	19.848 (2^{-7})	24.812 (2^{-29})	19.379 (2^{-5})	20.139 (2^{-7})	26.169 (2^{-26})
1	23.997 (2^{-4})	21.327 (2^{-6})	24.985 (2^{-28})	24.240 (2^{-2})	24.475 (2^{-6})	26.607 (2^{-22})
3	27.738 (2^{-2})	25.305 (2^{-8})	25.299 (2^{-8})	27.888 (2^{-1})	26.152 (2^{-7})	26.159 (2^{-7})
5	27.669 (2^{-3})	25.680 (2^{-8})	25.652 (2^{-8})	27.616 (2^{-2})	26.443 (2^{-7})	26.450 (2^{-7})

τ	“Resolution” phantom					
	non-whitened	whitened	12-K			
11-L	12-L	12-K	11-L	12-L	12-K	
0	29.713 (2^{-3})	29.488 (2^{-11})	31.356 (2^{-16})	29.812 (2^{-3})	29.512 (2^{-10})	31.766 (2^{-24})
1	30.765 (2^{-2})	29.534 (2^{-10})	31.697 (2^{-20})	30.990 (2^{-2})	30.248 (2^{-9})	32.391 (2^{-19})
3	31.634 (2^{-2})	30.426 (2^{-11})	31.376 (2^{-17})	31.707 (2^{-1})	30.875 (2^{-9})	31.554 (2^{-15})
5	31.510 (2^{-3})	30.432 (2^{-11})	31.806 (2^{-18})	31.544 (2^{-2})	31.243 (2^{-12})	31.753 (2^{-16})

Fig. 6: “Shape” phantom reconstructions, PSNR-optimized α according to Table I.

phantom for all τ thresholds and for the “resolution” phantom, also for large $\tau \geq 3$, whereas in the whitened case, we obtain analogous observations to the PSNR

case for both phantoms. For both phantoms, the overall best possible SSIM is obtained with 11-L in either non-whitened or whitened case.

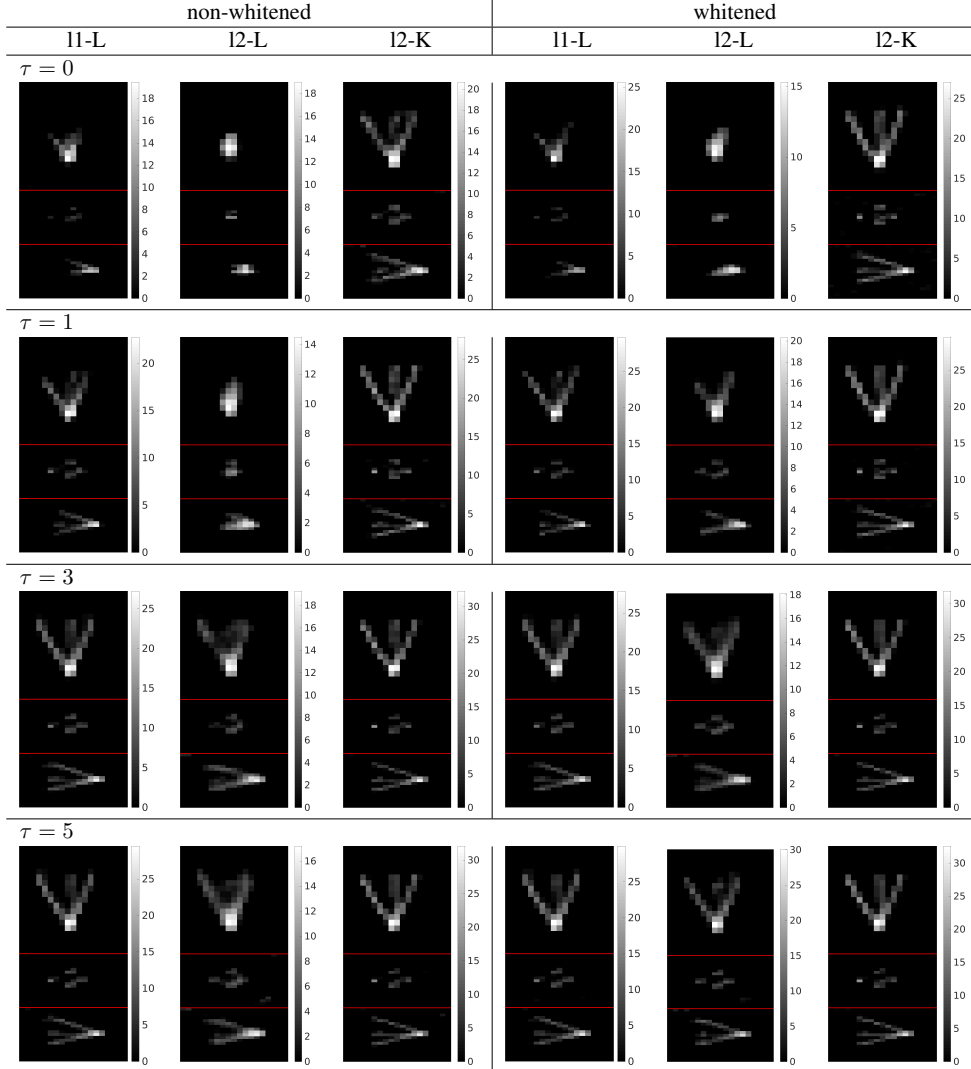


Fig. 7: “Resolution” phantom reconstructions, PSNR-optimized α according to Table I.

TABLE II: The ϵ_{SSIM} values for 11-L, 12-L, and 12-K (200 iterations).

τ	“Shape” phantom					
	non-whitened			whitened		
τ	11-L	12-L	12-K	11-L	12-L	12-K
0	0.607 (2^{-6})	0.543 (2^{-8})	0.606 (2^{-15})	0.606 (2^{-8})	0.591 (2^{-8})	0.677 (2^{-14})
1	0.709 (2^{-4})	0.606 (2^{-6})	0.635 (2^{-10})	0.711 (2^{-3})	0.705 (2^{-6})	0.728 (2^{-10})
3	0.810 (2^{-3})	0.689 (2^{-10})	0.687 (2^{-10})	0.792 (2^{-2})	0.704 (2^{-7})	0.704 (2^{-7})
5	0.692 (2^{-3})	0.575 (2^{-9})	0.599 (2^{-12})	0.706 (2^{-2})	0.614 (2^{-8})	0.645 (2^{-11})

τ	“Resolution” phantom					
	non-whitened			whitened		
τ	11-L	12-L	12-K	11-L	12-L	12-K
0	0.585 (2^{-3})	0.481 (2^{-10})	0.655 (2^{-17})	0.599 (2^{-4})	0.586 (2^{-10})	0.701 (2^{-15})
1	0.680 (2^{-5})	0.588 (2^{-10})	0.695 (2^{-17})	0.714 (2^{-27})	0.638 (2^{-10})	0.720 (2^{-13})
3	0.793 (2^{-2})	0.614 (2^{-12})	0.751 (2^{-14})	0.761 (2^{-1})	0.716 (2^{-10})	0.759 (2^{-14})
5	0.705 (2^{-2})	0.572 (2^{-14})	0.700 (2^{-14})	0.670 (2^{-1})	0.627 (2^{-11})	0.701 (2^{-14})

In contrast to the PSNR results, the reconstructions in Figs. 8 and 9 indicate less severe but still pronounced background artifacts for 12-K. For small thresholds, 12-L

fails to give reasonable results, while 11-L can give good reconstructions for $\tau \geq 1$. Similar to the PSNR case, for $\tau \geq 3$, 11-L yields reconstructions with sharper edges

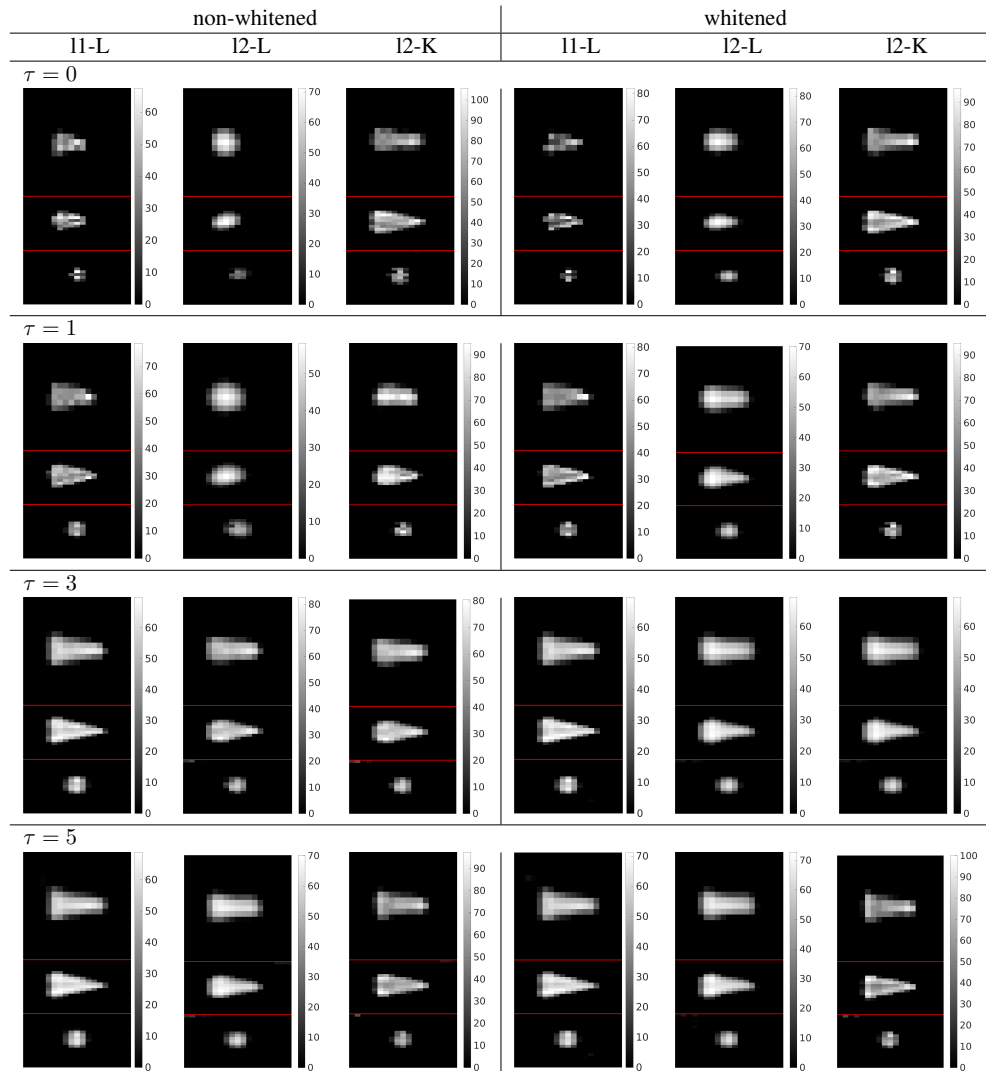


Fig. 8: “Shape” phantom reconstructions, SSIM-optimized α according to Table II.

and corners in the “shape” phantom. For the “resolution” phantom, I1-L and I2-K give similar results for $\tau \geq 3$, and both perform superior to I2-L.

Influence of SNR-threshold and general observations: Now we study the behavior of the quality measure with respect to the SNR threshold τ by examining Tables I and II columnwise more closely, since τ influences greatly the reconstruction. For PSNR, the observations vary dramatically across the methods. For I2-L, PSNR increases monotonically with τ in all cases, for I2-K, it does not show a steady trend, and for I1-L, it reaches a maximum before decreases again for $\tau = 5$. In contrast, SSIM in Table II first increases and then decrease for all methods in all cases. Thus, frequency selection with a proper τ benefits all methods and is recommended for MPI reconstruction, but a too large τ may compromise imaging quality, as observed earlier [23].

With whitening, for both phantoms, the performance of I2-L and I2-K can be improved, but I1-L benefits less from whitening in most cases. Statistically, whitening ensures that the i.i.d. assumption in the least-squares formulation is more adequately fulfilled (if the variance estimate is accurate), and thus it is more beneficial to the standard approach (II.4). I1-L is more resilient to noise type, and thus whitening plays a less important role. Surprisingly, visual inspection shows that whitening greatly improves the I1-L reconstruction in one case for the “resolution” phantom (cf. Fig. 10): it is the only one among all reconstructions that allows a clear distinction of all five capillaries in the x - z plane.

These observations indicate that solely I1 fitting without SNR thresholding is not able to compensate all data outliers. Visually inspecting Fig. 1 allows identifying severe outliers when no SNR-type thresholding is applied.

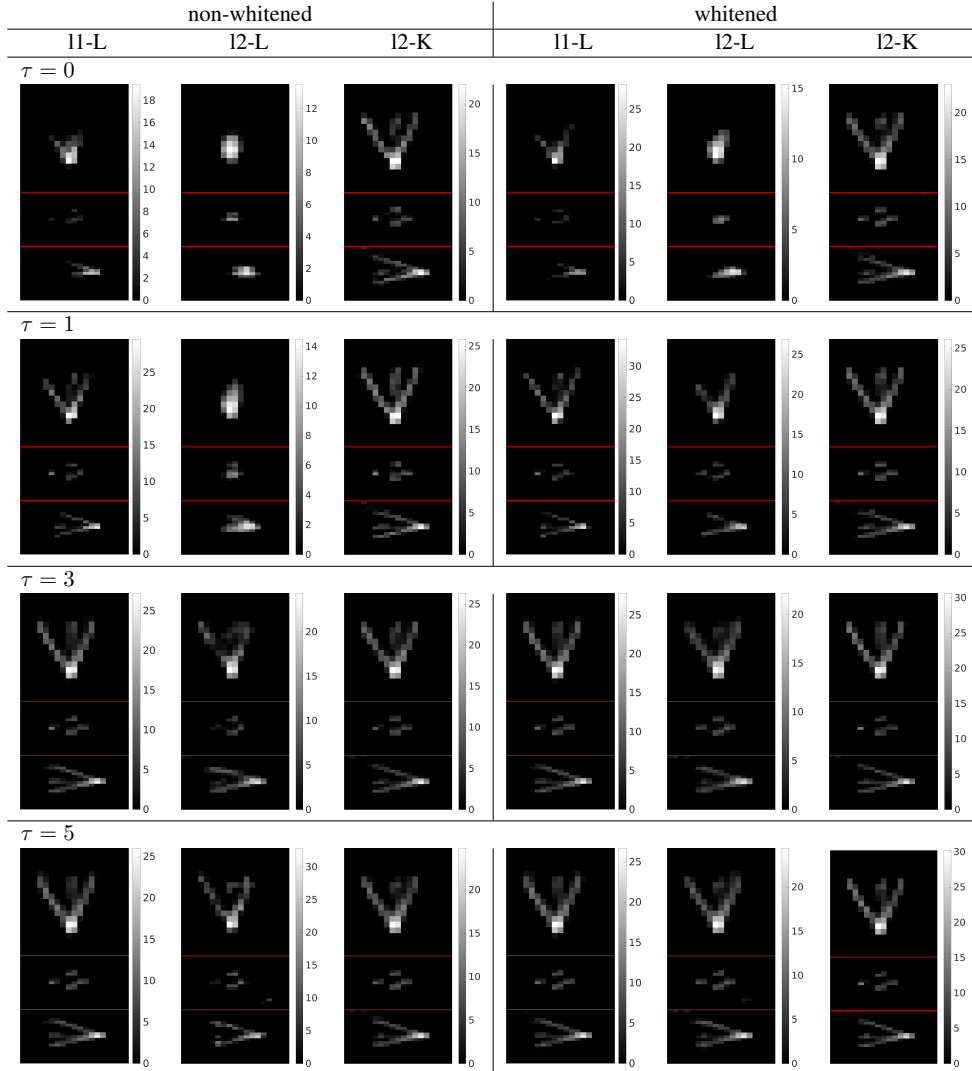


Fig. 9: “Resolution” phantom reconstructions, SSIM-optimized α according to Table II.

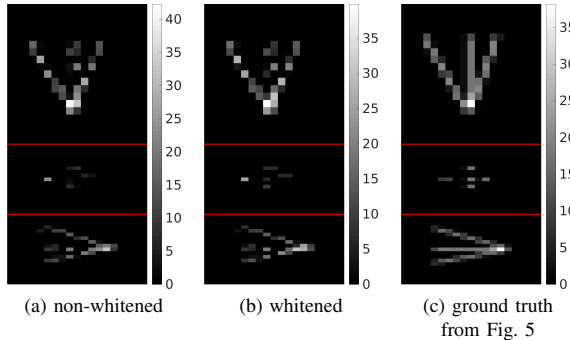


Fig. 10: “Resolution” phantom 11-L reconstruction for $\tau = 3$ and $\alpha = 2^{-13}$.

Thresholding still results in a background signal with a variance structure and large outliers, but the maximum

variance is several orders smaller in magnitudes than the no-thresholding case, cf. Fig. 2. In sum, frequency selection is beneficial for all methods when done carefully: A minimum τ is necessary but a too large τ can compromise image quality particularly in terms of SSIM.

B. Comparison with the standard approach

Now we present a more detailed comparative study of 11-L and 12-K, which is the one of the most commonly used techniques in MPI. Since within 12-K, there are two different sources of regularizing effect (i.e., variational and iterative), we test different iteration numbers K in 12-K to shed further insights, and present the PSNR and SSIM results in Tables III and IV. In almost all cases, we have a lower image quality measure for the 12-K cases in Tables I and II when compared with 12-K(50). In one exceptional case (SSIM, “resolution” phantom,

whitened) the image quality can be further improved by increasing K .

For the “shape” phantom, PSNR and SSIM results give rather different pictures. In terms of PSNR, one already obtains a superior value after one iteration (i.e., $K = 1$) compared to all other methods and K values, in both non-whitened and whitened cases. However, the SSIM values further increase with K . Nonetheless, $l1\text{-L}$ yields the best result in almost all cases under consideration, as observed earlier. This indicates the strong beneficial regularizing effect built into $l2\text{-K}$, and early stopping Kaczmarz iteration is competitive to $l2\text{-L}$, though at the expense of nontrivial stopping index. It is worth noting that the mechanism of the excellent performance of $l2\text{-K}$ with small τ (e.g. $\tau = 0, 1$, i.e., in the presence of severe outliers) is poorly understood. For the “resolution” phantom, the observations are more diffuse. In terms of PSNR, in the non-whitened case, the optimum is clearly achieved below $K = 200$ but varies greatly with τ . Provided that the optimal stopping index (and α) is found, $l2\text{-K}$ yields superior PSNR values. Similar observations hold in the whitened case. In terms of SSIM, the values further increase with K . Nonetheless, qualitative differences in the reconstructions are marginal for different K values, and for completeness, they are shown in Appendix A.

Finally, the computing time for the methods is summarized in Table V, which shows that computationally $l1\text{-L}$ is comparable with $l2\text{-K}(50)$. Note that in the literature the Kaczmarz method is also sometimes exploited for online reconstruction [19], [23]. This can be realized using a dimension reduction technique together with a sufficiently small number of iterations.

IV. CONCLUSIONS

In this work we have investigated the $l1$ data fitting for MPI reconstruction and compared it with the standard method in MPI. Without further preprocessing (except applying a bandpass filter) one can observe severe outliers in the MPI signal which are of orders of magnitudes larger and prevent obtaining reasonable reconstructions. A data fidelity term based on the $l1$ norm has been successfully applied to various applications, where the noise is characterized by severe outliers. However, within MPI, the $l1$ fitting can only solve the problem to a certain extent. We propose to combine it with the established SNR-type frequency selection (which still results in an MPI signal with large outliers). Then the $l1$ fitting method shows superior reconstruction performance for both non-whitened and whitened cases in terms of the popular PSNR and SSIM measures and visual quality. In particular, to the best of our knowledge, we have presented a first quantitative study on the phantom MPI data, which shows clearly the benefits of using $l1$ fitting.

In the context of $l2$ fitting, whitening is known to be ¹¹ beneficial for the reconstruction [23]. This suggests that whitening might adjust the noise characteristic such that it is closer to the i.i.d. Gaussian case, for which the $l2$ data fidelity is most suitable. This allows enhancing the reconstruction quality relevantly, which is confirmed by the numerical experiments. The influence of the $l1$ fitting is less dramatic due to its robustness with respect to outliers. There is strong implicit regularization built into the popular $l2\text{-K}$, whose precise mechanism is to be ascertained. Variational regularization methods need to carefully respect the MPI noise characteristic to be able to compete with $l2\text{-K}$, which is confirmed by the failure of $l2\text{-L}$ and the success of $l1\text{-L}$ for smaller SNR-thresholds. Besides MPI reconstructions, these findings also can have implications for the calibration procedure in the model-based approach. Whenever parameters in a suitable model has to be identified for the purpose of system calibration, the noise characteristic should be properly accounted for, e.g., using $l1$ fitting when using variational methods.

This study has only focused on the influence of the data fidelity, and does not touch the important issue of penalty for best possible image reconstruction. Advanced variational penalties [21], [50], e.g., $l1$, total variation and their variants and more recent learning based approaches [24], promise highly desirable features, e.g., edge preservation, at the expense of increased computational efforts, but largely remain to be systematically explored, naturally also with the $l1$ fitting. We leave these important issues to future works.

REFERENCES

- [1] T. Knopp, P. Szwargulski, F. Griese, and M. Gräser, “OpenMPI-Data: An initiative for freely accessible magnetic particle imaging data,” *Data in Brief*, vol. 28, pp. 104971, 7 pp., 2020.
- [2] B. Gleich and J. Weizenecker, “Tomographic imaging using the nonlinear response of magnetic particles,” *Nature*, vol. 435, no. 7046, pp. 1214–1217, 2005.
- [3] J. Weizenecker, B. Gleich, and J. Borgert, “Magnetic particle imaging using a field free line,” *J. Phys. D: Appl. Phys.*, vol. 41, no. 10, pp. 105009, 3 pp., 2008.
- [4] T. Knopp and T. M. Buzug, *Magnetic Particle Imaging: An Introduction to Imaging Principles and Scanner Instrumentation*. 2012: Springer. Heidelberg.
- [5] T. Knopp, N. Gdaniec, and M. Möddel, “Magnetic particle imaging: from proof of principle to preclinical applications,” *Phys. Med. Biol.*, vol. 62, no. 14, pp. R124–R178, 2017.
- [6] T. Kluth, “Mathematical models for magnetic particle imaging,” *Inverse Problems*, vol. 34, no. 8, pp. 083001, 27 pp., 2018.
- [7] J. Weizenecker, B. Gleich, J. Rahmer, H. Dahnke, and J. Borgert, “Three-dimensional real-time *in vivo* magnetic particle imaging,” *Phys. Med. Biol.*, vol. 54, no. 5, pp. L1–L10, 2009.
- [8] A. P. Khandhar, P. Keselman, S. J. Kemp, R. Ferguson, P. Goodwill, S. Conolly, and K. Krishnan, “Evaluation of PEG-coated iron oxide nanoparticles as blood pool tracers for preclinical magnetic particle imaging,” *Nanoscale*, vol. 9, no. 3, pp. 1299–1306, 2017.

TABLE III: The ϵ_{PSNR} values for l2-K with varying iteration numbers in parentheses.

τ	“Shape” phantom			“Resolution” phantom		
	non-whitened			whitened		
(50)	(20)	(1)	(50)	(20)	(1)	
0	25.581 (2^{-14})	27.087 (2^{-15})	28.469 (2^{-17})	26.487 (2^{-13})	27.961 (2^{-13})	29.112 (2^{-16})
1	26.351 (2^{-15})	27.703 (2^{-13})	28.748 (2^{-15})	26.754 (2^{-20})	28.069 (2^{-11})	29.431 (2^{-13})
3	25.737 (2^{-9})	26.889 (2^{-12})	28.920 (2^{-14})	26.127 (2^{-7})	27.381 (2^{-10})	29.269 (2^{-13})
5	26.240 (2^{-10})	27.195 (2^{-12})	28.619 (2^{-15})	26.480 (2^{-8})	27.479 (2^{-10})	28.910 (2^{-13})

τ	“Shape” phantom			“Resolution” phantom		
	non-whitened			whitened		
(50)	(20)	(1)	(50)	(20)	(1)	
0	31.580 (2^{-16})	31.456 (2^{-16})	31.673 (2^{-18})	31.777 (2^{-22})	31.793 (2^{-20})	31.880 (2^{-17})
1	31.811 (2^{-18})	31.767 (2^{-18})	31.747 (2^{-16})	32.390 (2^{-16})	32.242 (2^{-16})	31.922 (2^{-14})
3	31.831 (2^{-17})	31.881 (2^{-17})	31.656 (2^{-15})	32.131 (2^{-15})	32.142 (2^{-16})	31.724 (2^{-14})
5	32.149 (2^{-18})	31.965 (2^{-19})	31.418 (2^{-17})	32.133 (2^{-16})	32.065 (2^{-17})	31.413 (2^{-15})

TABLE IV: The ϵ_{SSIM} values for l2-K with varying iteration numbers in parentheses.

τ	“Shape” phantom			“Resolution” phantom		
	non-whitened			whitened		
(50)	(20)	(1)	(50)	(20)	(1)	
0	0.630 (2^{-12})	0.588 (2^{-12})	0.288 (2^{-15})	0.695 (2^{-12})	0.686 (2^{-11})	0.294 (2^{-15})
1	0.697 (2^{-9})	0.680 (2^{-7})	0.296 (2^{-13})	0.784 (2^{-8})	0.755 (2^{-6})	0.301 (2^{-12})
3	0.653 (2^{-10})	0.610 (2^{-13})	0.311 (2^{-12})	0.705 (2^{-7})	0.685 (2^{-11})	0.307 (2^{-11})
5	0.645 (2^{-14})	0.672 (2^{-13})	0.305 (2^{-12})	0.649 (2^{-9})	0.626 (2^{-13})	0.301 (2^{-11})

τ	“Shape” phantom			“Resolution” phantom		
	non-whitened			whitened		
(50)	(20)	(1)	(50)	(20)	(1)	
0	0.638 (2^{-15})	0.587 (2^{-14})	0.292 (2^0)	0.689 (2^{-15})	0.654 (2^{-14})	0.347 (2^0)
1	0.697 (2^{-15})	0.662 (2^{-14})	0.259 (2^0)	0.707 (2^{-12})	0.678 (2^{-12})	0.274 (2^{-12})
3	0.710 (2^{-16})	0.700 (2^{-15})	0.281 (2^0)	0.724 (2^{-12})	0.692 (2^{-11})	0.282 (2^{-11})
5	0.709 (2^{-16})	0.695 (2^{-15})	0.309 (2^{-11})	0.697 (2^{-12})	0.683 (2^{-13})	0.303 (2^{-10})

TABLE V: The mean and standard deviation of computing times are computed over 30 α values and 2 phantoms. The number in the bracket is the iteration number for l2-K. Computations are carried out on a server with 2 \times Intel® Xeon® Broadwell-EP Series Processor E5-2687W v4, 3.00 GHz, 12-Core, and 1.5 TB DDR4 PC2666 main memory.

τ	non-whitened			whitened		
	11-L	12-K(200)	(50)	(20)	(1)	
0	71.09 ± 91.46	556.64 ± 12.21	140.78 ± 3.66	58.96 ± 1.84	7.08 ± 0.25	
1	125.60 ± 151.77	547.17 ± 11.74	137.53 ± 3.54	57.25 ± 1.88	6.92 ± 0.26	
3	43.30 ± 26.91	78.60 ± 2.87	19.74 ± 0.72	8.19 ± 0.26	0.96 ± 0.02	
5	33.51 ± 17.32	48.62 ± 2.57	12.64 ± 0.46	5.34 ± 0.22	0.66 ± 0.02	

τ	non-whitened			whitened		
	11-L	12-K(200)	(50)	(20)	(1)	
0	23.63 ± 21.44	552.91 ± 9.69	139.68 ± 3.52	58.82 ± 1.93	7.27 ± 0.24	
1	113.24 ± 130.26	544.22 ± 10.16	137.10 ± 3.14	57.43 ± 1.81	6.97 ± 0.32	
3	48.61 ± 25.53	78.37 ± 2.44	19.59 ± 0.78	8.14 ± 0.28	0.97 ± 0.02	
5	34.11 ± 17.21	48.61 ± 1.96	12.60 ± 0.47	5.30 ± 0.22	0.65 ± 0.03	

- [9] J. Franke, R. Lacroix, H. Lehr, M. Heidenreich, U. Heinen, and V. Schulz, “Mpi flow analysis toolbox exploiting pulsed tracer information an aneurysm phantom proof,” *Int. J. Magnet. Part. Imag.*, vol. 3, no. 1, pp. 703–020, 5 pp., 2017.
- [10] J. Haegele, J. Rahmer, B. Gleich, J. Borgert, H. Wojtczyk, N. Panagiotopoulos, T. Buzug, J. Barkhausen, and F. Vogt, “Magnetic particle imaging: visualization of instruments for cardiovascular intervention,” *Radiology*, vol. 265, no. 3, pp. 933–938, 2012.
- [11] J. Salamon, M. Hofmann, C. Jung, M. G. Kaul, F. Werner, K. Them, R. Reimer, P. Nielsen, A. vom Scheidt, G. Adam, T. Knopp, and H. Ittrich, “Magnetic particle/magnetic resonance imaging: in-vitro MPI-guided real time catheter tracking and 4D angioplasty using a road map and blood pool tracer approach,” *PLOS One*, vol. 11, no. 6, pp. e0156899–14, 2016.
- [12] E. Y. Yu, M. Bishop, B. Zheng, R. M. Ferguson, A. P. Khandhar, S. J. Kemp, K. M. Krishnan, P. W. Goodwill, and S. M. Conolly, “Magnetic particle imaging: A novel in vivo imaging platform for cancer detection,” *Nano Letters*, vol. 17, no. 3, pp. 1648–1654, 2017.
- [13] K. Murase, M. Aoki, N. Banura, K. Nishimoto, A. Mimura, T. Kuboyabu, and I. Yabata, “Usefulness of magnetic particle imaging for predicting the therapeutic effect of magnetic hyperthermia,” *Open J. Med. Imag.*, vol. 5, no. 2, p. 85, 2015.
- [14] J. Rahmer, J. Weizenecker, B. Gleich, and J. Borgert, “Signal encoding in magnetic particle imaging: properties of the system function,” *BMC Med. Imag.*, vol. 9, no. 4, p. 21 pp., 2009.
- [15] T. Knopp, J. Rahmer, T. F. Sattel, S. Biederer, J. Weizenecker, B. Gleich, J. Borgert, and T. M. Buzug, “Weighted iterative reconstruction for magnetic particle imaging,” *Phys. Med. Biol.*,

vol. 55, no. 6, pp. 1577–1589, 2010.

[16] P. W. Goodwill and S. M. Conolly, “Multidimensional x-space magnetic particle imaging,” *IEEE Trans. Med. Imag.*, vol. 30, no. 9, pp. 1581–1590, 2001.

[17] P. W. Goodwill, E. U. Saritas, L. R. Croft, T. N. Kim, K. M. Krishnan, D. V. Schaffer, and S. M. Conolly, “X-space MPI: magnetic nanoparticles for safe medical imaging,” *Adv. Mater.*, vol. 24, no. 28, pp. 3870–3877, 2012.

[18] J. Rahmer, A. Halkola, B. Gleich, I. Schmale, and J. Borgert, “First experimental evidence of the feasibility of multi-color magnetic particle imaging,” *Phys. Med. Biol.*, vol. 60, no. 5, pp. 1775–1791, 2015.

[19] T. Knopp and M. Hofmann, “Online reconstruction of 3D magnetic particle imaging data,” *Phys. Med. Biol.*, vol. 61, no. 11, pp. N257–67, 2016.

[20] M. Storath, C. Brandt, M. Hofmann, T. Knopp, J. Salamon, A. Weber, and A. Weinmann, “Edge preserving and noise reducing reconstruction for magnetic particle imaging,” *IEEE Trans. Med. Imag.*, vol. 36, no. 1, pp. 74–85, 2017.

[21] T. Kluth and P. Maass, “Model uncertainty in magnetic particle imaging: Nonlinear problem formulation and model-based sparse reconstruction,” *Int. J. Magnetic Part. Imag.*, vol. 3, no. 2, pp. 1707004, 10 pp., 2017.

[22] C. Brandt and A. Seppänen, “Recovery from errors due to domain truncation in magnetic particle imaging: Approximation error modeling approach,” *J. Math. Imag. Vis.*, vol. 60, no. 8, pp. 1196–1208, 2018.

[23] T. Kluth and B. Jin, “Enhanced reconstruction in magnetic particle imaging by whitening and randomized svd approximation,” *Phys. Med. Biol.*, vol. 64, no. 12, pp. 125026, 21 pp., 2019.

[24] S. Dittmer, T. Kluth, P. Maass, and D. O. Baguer, “Regularization by architecture: A deep prior approach for inverse problems,” *J. Math. Imag. Vis.*, p. in press, 2019.

[25] T. Kluth, B. Jin, and G. Li, “On the degree of ill-posedness of multi-dimensional magnetic particle imaging,” *Inverse Problems*, vol. 34, no. 9, pp. 095006, 26 pp., 2018.

[26] S. Kaczmarz, “Angenäherte auflösung von Systemen linearer Gleichungen,” *Bull. Int. Acad. Pol. Sci. Lett. A*, vol. 35, pp. 335–357, 1937.

[27] T. Kluth, P. Szwargulski, and T. Knopp, “Towards accurate modeling of the multidimensional magnetic particle imaging physics,” *New Journal of Physics*, vol. 21, no. 10, p. 103032, 2019.

[28] S. Alliney and S. Ruzinsky, “An algorithm for the minimization of mixed 11 and 12 norms with application to Bayesian estimation,” *IEEE Trans. Signal Process.*, vol. 42, no. 3, pp. 618–627, 1994.

[29] C. Clason, B. Jin, and K. Kunisch, “A semismooth Newton method for L^1 data fitting with automatic choice of regularization parameters and noise calibration,” *SIAM J. Imaging Sci.*, vol. 3, no. 2, pp. 199–231, 2010.

[30] A. Gelman, J. B. Carlin, H. S. Stern, and D. B. Rubin, *Bayesian Data Analysis*, 2nd ed. CRC, Boca Raton, FL, 2004.

[31] R. H. Byrd, P. Lu, J. Nocedal, and C. Y. Zhu, “A limited memory algorithm for bound constrained optimization,” *SIAM J. Sci. Comput.*, vol. 16, no. 5, pp. 1190–1208, 1995.

[32] C. Zhu, R. H. Byrd, P. Lu, and J. Nocedal, “Algorithm 778: L-BFGS-B: Fortran subroutines for large-scale bound-constrained optimization,” *ACM Trans. Math. Software*, vol. 23, no. 4, pp. 550–560, 1997.

[33] J. Franke, U. Heinen, H. Lehr, A. Weber, F. Jaspard, W. Ruhn, M. Heidenreich, and V. Schulz, “System characterization of a highly integrated preclinical hybrid MPI-MRI scanner,” *IEEE Trans. Med. Imag.*, vol. 35, no. 9, pp. 1993–2004, 2016.

[34] K. Ito and B. Jin, *Inverse Problems: Tikhonov Theory and Algorithms*. World Scientific, Hackensack, NJ, 2015.

[35] K. Them, M. G. Kaul, C. Jung, M. Hofmann, T. Mummert, F. Werner, and T. Knopp, “Sensitivity enhancement in magnetic particle imaging by background subtraction,” *IEEE Trans. Med. Imag.*, vol. 35, no. 3, pp. 893–900, 2016.

[36] M. Straub and V. Schulz, “Joint reconstruction of tracer distribution and background in magnetic particle imaging,” *IEEE Trans. Med. Imag.*, vol. 37, no. 5, pp. 1192–1203, 2018.

[37] T. Knopp, G. N. R. Rehr, M. Graeser, and T. Germann, “Correction of linear system drifts in magnetic particle imaging,” *Phys. Med. Biol.*, vol. 64, no. 12, p. 125013, 2019.

[38] J. Weizenecker, J. Borgert, and B. Gleich, “A simulation study on the resolution and sensitivity of magnetic particle imaging,” *Phys. Med. Biol.*, vol. 52, no. 21, pp. 6363–6374, 2007.

[39] I. Schmale, B. Gleich, J. Borgert, and J. Weizenecker, “Noise within magnetic particle imaging,” in *Magnetic Nanoparticles*, T. M. Buzug, J. Borgert, T. Knopp, T. F. Biederer, Sattel, M. Erbe, and K. Lüdtke-Buzug, Eds., 2010, pp. 154–161.

[40] A. C. Bovik, Ed., *Handbook of Image and Video Processing*. London: Elsevier, Academic Press, 2010.

[41] P. J. Huber, *Robust Statistics*. John Wiley & Sons, Inc., New York, 1981.

[42] H. Hwang and R. A. Haddad, “Adaptive median filters: new algorithms and results,” *IEEE Trans. Imag. Proc.*, vol. 4, no. 4, pp. 499–502, 1995.

[43] A. Buades, B. Coll, and J.-M. Morel, “Nonlocal image and movie denoising,” *Int. J. Comput. Vis.*, vol. 76, no. 2, pp. 123–139, 2008.

[44] S. Foss, D. Korshunov, and S. Zachary, *An Introduction to Heavy-Tailed and Subexponential Distributions*. New York: Springer, 2013.

[45] P. Rodríguez and B. Wohlberg, “Efficient minimization method for a generalized total variation functional,” *IEEE Trans. Image Process.*, vol. 18, no. 2, pp. 322–332, 2009.

[46] J. Yang and Y. Zhang, “Alternating direction algorithms for ℓ_1 -problems in compressive sensing,” *SIAM J. Sci. Comput.*, vol. 33, no. 1, pp. 250–278, 2011.

[47] T. Knopp, T. Viereck, G. Bringout, M. Ahlborg, J. Rahmer, and M. Hofmann, “MDF: Magnetic particle imaging data format,” Preprint, arXiv:1602.06072, 2016.

[48] A. Horá and D. Ziou, “Image quality metrics: PSNR vs. SSIM,” in *20th International Conference on Pattern Recognition*, 2010, pp. 2366–2369.

[49] H. W. Engl, M. Hanke, and A. Neubauer, *Regularization of Inverse Problems*. Kluwer, Dordrecht, 1996.

[50] S. İlbey, C. B. Top, A. Güngör, T. Çukur, E. U. Saritas, and H. E. Güven, “Fast system calibration with coded calibration scenes for magnetic particle imaging,” *IEEE Trans. Med. Imag.*, vol. 38, no. 9, pp. 2070–2080, 2019.

APPENDIX A
SUPPLEMENTARY MATERIAL: COMPARISON WITH THE STANDARD APPROACH

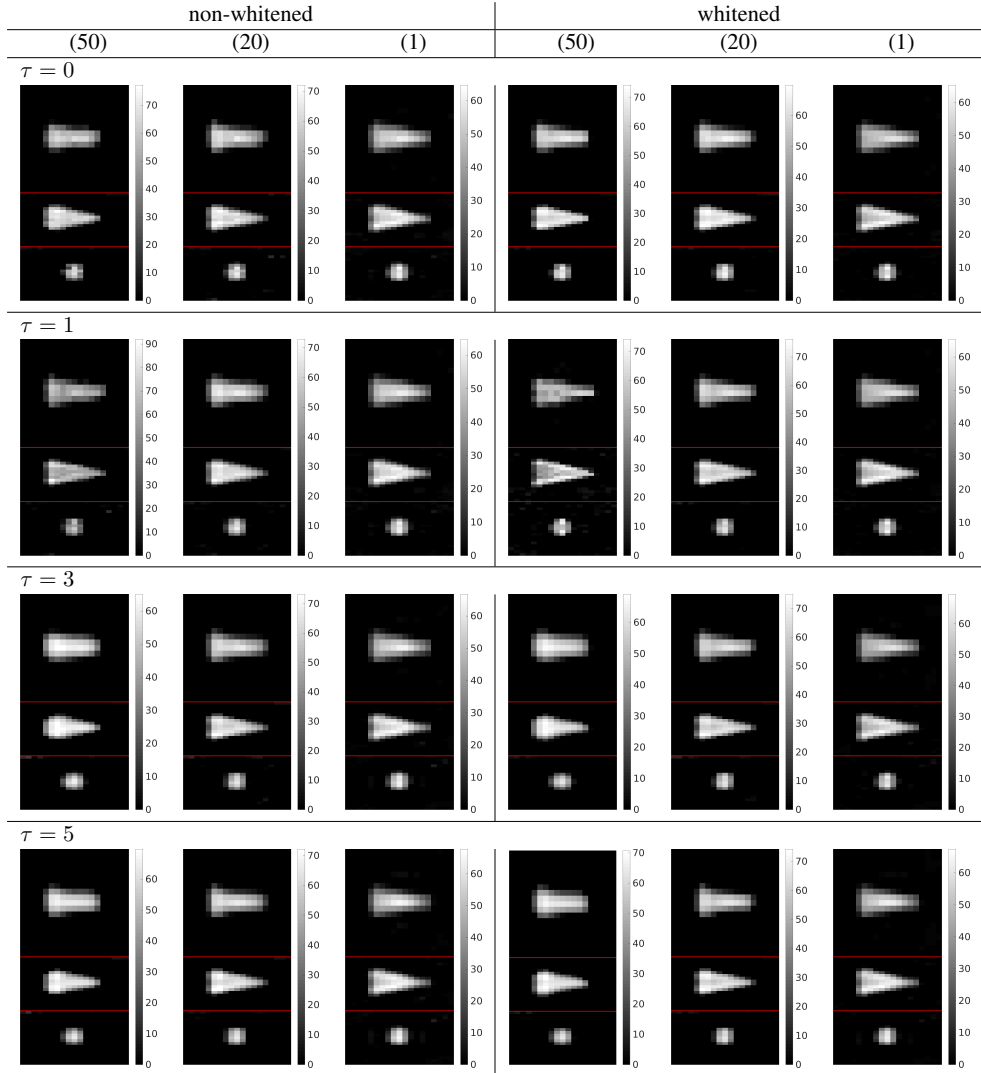
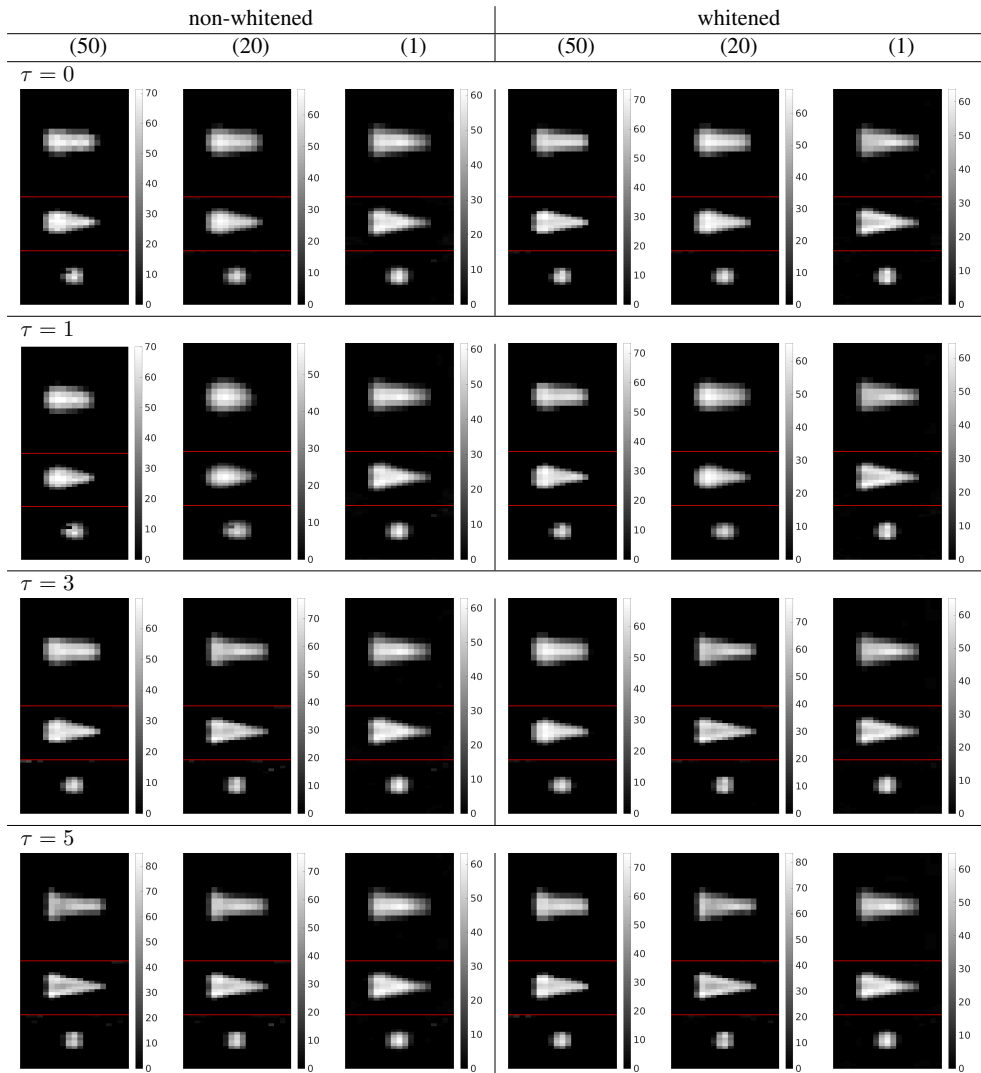


Fig. 11: “Shape” phantom reconstructions, PSNR-optimized α according to Table III.



Fig. 12: “Resolution” phantom reconstructions, PSNR-optimized α according to Table III.

Fig. 13: “Shape” phantom reconstructions, SSIM-optimized α according to Table IV.

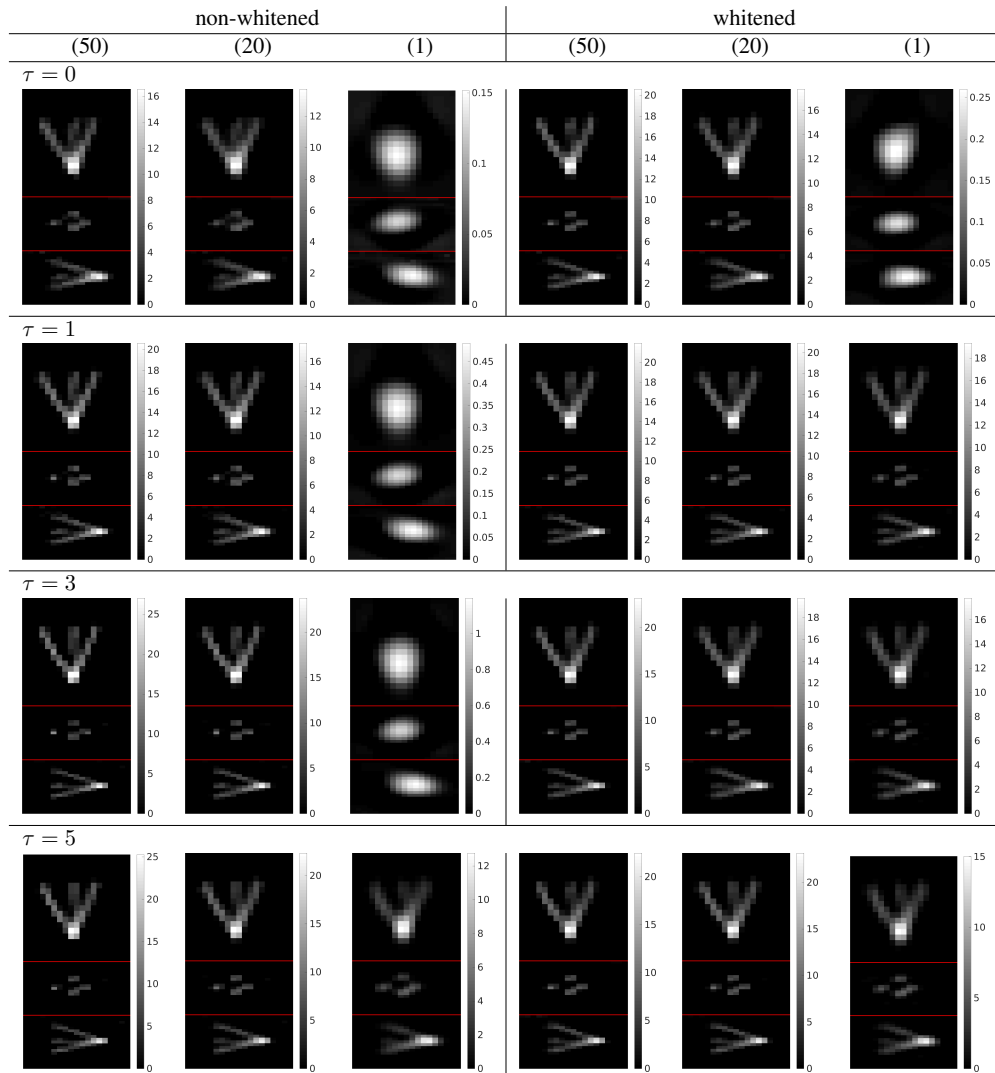


Fig. 14: “Resolution” phantom reconstructions, SSIM-optimized α according to Table IV.